

# Neutral and stratified turbulent boundary layer flow over low mountains

Francois Lott<sup>1\*</sup> | Anton Beljaars<sup>2†</sup> | Lucile Pauget<sup>1,3‡</sup>  
| Bruno Deremble<sup>4‡</sup>

<sup>1</sup>Universite PSL, Ecole Normale Supérieure, Département des géosciences, Laboratoire de Météorologie Dynamique, Paris France

<sup>2</sup>European Centre for Medium-Range Weather Forecasts, Reading, UK

<sup>3</sup>Commissariat à l'Energie atomique/DAM, Bruyères le Chatel, France

<sup>4</sup>University Grenoble Alpes, Grenoble, France

## Correspondence

Francois Lott, Laboratoire de Météorologie Dynamique, Ecole Normale Supérieure, 24 rue Lhomond, 75231 Paris France  
Email:

## Funding information

VESRI Schmidt Future project DataWave; Laboratoire de Recherche Conventionné "Yves Rocard," a collaborative unit between CEA and ENS.

A theory for flow over gentle hills using a mixing length turbulence closure is developed to describe the transition from turbulent orographic form drag to gravity wave drag. It confirms that the first is associated with downstream sheltering, the second with upstream blocking and strong down-slope winds. It shows that the altitude at which the incident flow needs to be taken to calculate the drag is the inner layer scale at which dissipation equilibrates disturbance advection. It also shows that the parameter that controls the transition, here a Richardson number, compares the mountain length to the altitude of the turning points above which the upward propagating gravity waves become evanescent.

Our solutions are also used to show that the down-slope winds penetrate well into the inner layer and that a good fraction of the drag is deposited in the inner layer: all of it in the neutral case, a large fraction in the intermediate cases when there are trapped lee waves, and even in stable situations without trapping part of the gravity wave drag is eroded in the inner layer. Some discussion on how to combine neutral and stratified effects in the parameterization of subgrid scale orography in large-scale models is given.

---

\* Conceptualization, Formal analysis, Methodology, Writing

† Conceptualization, Methodology, Writing

‡ Software, Validation

**KEYWORDS**

Mountain waves, Neutral and stratified boundary layers, Sheltering effect, flow blocking, Mountain drag, Reynolds stress

**1 | INTRODUCTION**

2 Topographies with small horizontal scale  $L$  are assumed to produce disturbances with amplitude exponentially decay-  
3 ing in the free atmosphere (evanescent waves), hence essentially affecting the boundary layer. The modification of  
4 turbulent dissipation (and induced stress) results in mountain drag forces that can substantially increase the turbulent  
5 drag (Hunt et al., 1988a). In this case the drag is related to downstream "non-separated" sheltering with the pressure  
6 loss across the hill being caused by frictional retardation of the flow near the surface when the slopes are sufficiently  
7 small or by flow separation on the downstream side when the slopes are large (see for instance the Large-Eddy Simula-  
8 tions – LES – in Allen and Brown (2002) and Reinert et al. (2007)). A pretty illustration of such downstream separation  
9 and the associated circulations is the formation of banner clouds which sometimes appear in the right conditions  
10 (Voigt and Wirth, 2013). For mountains with bigger horizontal length scale and in the presence of stratification, buoy-  
11 ancy force can act against downstream sheltering, forcing an intense flow along the downstream flank of the hill. The  
12 mechanism at work in this case is related to buoyancy/gravity waves, and is efficient for two reasons. The first reason  
13 is that in the presence of internal waves the disturbance amplitudes no longer decay exponentially with altitude in  
14 the free atmosphere, which means that the dynamics is no longer limited to the boundary layer. The second reason is  
15 that close to the surface, the horizontal and vertical wind have opposite phase, i.e large horizontal wind occurs when  
16 the vertical velocity is negative, which is the fundamental mechanism causing downslope winds (see more details  
17 in the review by Durran (1990)). Still in these conditions, the wind also becomes weak upstream, causing upstream  
18 blocking for large mountains (some recent observations and LES simulations are in Pokharel et al. (2017) and Sauer  
19 et al. (2016)). In these stratified cases, the drag is caused by mountain waves for low hills, and blocked flow drag for  
20 mountains of sufficient height.

21 Although these contrasting dynamics can be studied in great detail using high resolution models (Finnigan et al.,  
22 2020), the transition between the two regimes has not received much attention. To our knowledge, only a few papers  
23 address this transition explicitly. Belcher and Wood (1996) analyse theoretically the transition from form drag to  
24 wave drag, the form drag being related to non-separated sheltering gradually being replaced by wave drag when  
25 stratification increases. The transition has also been analysed in wind-tunnel experiments and numerical simulations  
26 by Ross et al. (2004) or in the prediction of where flow separation is likely to occur (Ambaum and Marshall, 2005).  
27 The fact that the transition itself is not much studied, does not mean that the interplay between boundary layers and  
28 mountain waves has never been analysed. Numerous papers analyse the impact of the boundary layer on mountain  
29 waves (Richard et al., 1989; Smith et al., 2006) or on the trapped waves developing at a boundary layer inversion  
30 (Teixeira et al., 2013a; Sachsperger et al., 2015). The fact that some wave drag in the boundary layer can be significant  
31 was also recognized by Tsiringakis et al. (2017) and earlier by Chimonas and Nappo (1989). Beyond the drag itself,  
32 the contribution of boundary layer waves to turbulent exchange is also recognized in oceanography and for sediment  
33 suspension (Boegman and Stastna, 2019; Soontiens et al., 2015).

34 The purpose of this study is to re-visit early theories about the interactions between mountain and boundary layer  
35 in the neutral and stratified case. For this purpose we return to theories dating back from the 80-90's (Hunt et al.,  
36 1988a; Belcher and Wood, 1996; Hunt et al., 1988b) and complement them by deriving uniform approximations that  
37 capture smoothly the transitions between the so-called "inner" and "outer" regions. As we will see, the solutions

we obtain capture all together the rich quasi-"inviscid" dynamics associated with the conventional mountain wave theory (which includes trapped lee-waves) and its explicit interaction with the boundary layer dynamics (for instance the extent to which downslope winds penetrate into the inner layer). Our study also has a more practical motivation: there are two families of subgrid scale orography parameterizations in present day weather forecast and climate models. A first family represents the enhancement of turbulent drag by orography (Wood and Mason, 1993), with parameterizations that are today improved to represent better nonlinear effects and the vertical distribution of the drag (Wood et al., 2001; Beljaars et al., 2004). A second family represents a dynamics controlled by gravity waves (Palmer et al., 1986) and that has also been extended to include nonlinear effects (Lott and Miller, 1997). It is generally assumed that the first type of parameterization, also called TOFD for "turbulent orographic form drag" should act for mountains of scale  $L < 5$  km typically, whereas the second type also called SSO for "subgrid scale orography" should consider large-scale mountains (Beljaars et al., 2004). With increasing model resolution it could be argued that only the TOFD parameterizations should stay in the future, the gravity wave part being explicitly resolved, but we are probably still far from this status. A first reason is that the effective resolution of weather forecast models can be near an order of magnitude coarser than the model grid size (Vosper et al., 2016). A second reason is that the  $L = 5$  km cutoff is quite arbitrary and should be determined according to the local condition before removing the SSO-type schemes. A third reason is that even if a model can potentially resolve the small-scale gravity waves, they will certainly interact with some form of turbulent parameterization: understanding theoretically the interaction remains important.

In a recent series of papers, Lott et al. (2020a,b) and Soufflet et al. (2022) (hereinafter Part I, Part II, and Part III), formulated such theory and presented uniform solutions in the constant eddy viscosity case for small slopes  $S$ . They show that the disturbance amplitude is near that predicted using inviscid theory if one takes for incident wind its value at altitude near the inner layer scale  $\delta$  where dissipative effects equilibrate disturbance advection,

$$\frac{U_0(\delta)}{L} \approx \frac{v'(\delta)}{\delta^2}, \quad (1)$$

$U_0$  and  $v'$  being the incident wind and the eddy diffusivity acting on the disturbance respectively. Part II then describes the transition from neutral to stratified and shows that the transition occurs when the Richardson number  $J \approx 1$ . To interpret this result they estimated in their Eq. (33) the turning point altitude where the Scorer parameter satisfies

$$S_c(h_t) = \frac{N(h_t)^2}{U(h_t)^2} - \frac{U_{zz}(h_t)}{U(h_t)} = 1/L^2, \quad (2)$$

$h_t$  being the altitude above which the disturbance with wavenumber  $1/L$  becomes evanescent in the vertical direction. In Part II the turning level was found to be approximately at  $h_t \approx \sqrt{J} L$ . With  $J < 1$  ( $J > 1$ ) the turning level is close to (far from) the surface compared to the mountain length, and we argued that the gravity waves have not (have) enough vertical space to develop and the dynamics is neutral (stratified). When the wind is sheared in the boundary layer and becomes constant above, we found in part III that the Richardson number in the boundary layer, but above the inner layer is still the appropriate parameter to estimate the nature of the dynamics. In all cases we found that the transition from neutral to stratified is also a transition from downstream sheltering to upstream blocking when the height of the mountain approaches the inner layer scale (Part II and III). Part III also revealed the significance of the trapped lee waves during the transition (when  $J \approx 1$ ) and the redistribution of the pressure drag in terms of vertical and horizontal pseudo momentum flux.

Since the constant viscosity model is too simple to represent the real eddy diffusivity, particularly its decay when approaching the surface, the purpose of the present paper is to extend the formalism in Part I, Part II and Part III by using a first order mixing length closure reminiscent of the one used in Belcher and Wood (1996).

75 The plan of the paper is as follows. In section 2, we recall the basic equations and give an outline of the theory used  
 76 in comparison to the theories used in the past. In section 3, we describe the transition from downstream sheltering  
 77 to upstream blocking and describe the trapped waves that strongly develop during the transition. In section 4, we  
 78 present diagnostics of mountain drag and Reynolds stresses profiles. In section 5, we summarize and discuss the  
 79 significance of our results in the context of subgrid scale orography parameterization. We also relate them to the  
 80 results in Belcher and Wood (1996). The model is detailed in the Appendix, it combines asymptotic developments  
 81 and numerical integrations of the inner layer equations using a curved coordinate formalism.

## 82 2 | BASIC EQUATIONS

### 83 2.1 | Boussinesq equations and mixing length

84 All our calculations use the Boussinesq approximation written in hybrid terrain following coordinates  $(X, Z)$  which  
 85 are related to the Cartesian coordinates  $(x, z)$  via,

$$x = X, \quad z = Z + h(X)f(Z) = Z + z', \quad (3)$$

86 where  $h(x)$  is the mountain height and the function  $f(Z)$  is positive.  $f(Z)$  ensures the transition from terrain fol-  
 87 lowing coordinates near the surface to Cartesian coordinates by taking  $f(0) = 1$  and decaying towards 0 for  $Z \rightarrow \infty$ .  
 88 From Eqs. (2.21)-(2.28) and (3.18)-(3.20) in Clark (1977), it can be shown that the stationary Boussinesq equations  
 89 can be written,

$$\rho (u \partial_X u + W \partial_Z u) = -(\partial_X \rho p + \partial_Z \rho g^{12} \rho) + \partial_Z \tau_{XZ}, \quad (4a)$$

$$\rho (u \partial_X w + W \partial_Z w) = -\partial_Z p + \rho b + \partial_Z \tau_{XZ}, \quad (4b)$$

$$\rho (u \partial_X b + W \partial_Z b) = \partial_Z q_Z, \quad (4c)$$

$$\partial_X \rho u + \partial_Z \rho W = 0, \quad (4d)$$

93 where the "pseudo" density  $\rho$  is the Jacobian of the coordinate transformation,  $\rho g^{12}$  is a metric tensor coefficient,  
 94 and  $W$  a velocity in the direction perpendicular to the  $Z = \text{constant}$  surfaces:

$$\rho = \partial_Z Z, \quad \rho g^{12} = -\partial_X Z, \quad W = u \partial_X Z + w \partial_Z Z, \quad (5)$$

95  $u$  and  $w$  being the horizontal and vertical velocities. Compared to Clark (1977) we have rather followed the common  
 96 practice to neglect the stresses and heat flux in the horizontal direction ( $\tau_{XX}$ ,  $\tau_{ZX}$ , and  $q_X$ ), which is consistent with  
 97 the mixing length model we will adopt. Finally in (4) we have divided pressure anomaly by a constant reference density  
 98  $\rho_s \left( \frac{p - p_s(z)}{\rho_s} \rightarrow p \right)$  and the buoyancy  $b = -g \frac{\theta - \theta_s}{\theta_s}$ ,  $\theta$  being potential temperature and  $\theta_s$  a reference value.

99 In general, we will assume no slip and no flow boundary conditions at the surface:

$$u(Z=0) = W(Z=0) = b(Z=0) = 0. \quad (6)$$

100 To express the stress tensors, we use a closure for eddy diffusivity based on mixing length theory,

$$\tau_{XZ} = \nu \partial_Z u, \quad \tau_{ZZ} = \nu \partial_Z w, \quad \text{and } q_Z = \nu \partial_Z b \text{ with } \nu = \Lambda_0^2 \left\| \frac{\partial u}{\partial Z} \right\|, \quad (7)$$

101 where  $\Lambda_0$  is the mixing length. Standard atmospheric boundary layer models for neutral flow often have a smooth  
102 transition from the linear increase of mixing length near the surface to a constant limit value  $\lambda$  far away from the  
103 surface, for instance according to the so-called Blackadar formulation.

$$\frac{1}{\Lambda_0} = \frac{1}{\kappa(Z+z_0)} + \frac{1}{\lambda}, \quad (8)$$

104 where  $\kappa$  is the von Karman constant and  $z_0$  a roughness length. As  $\lambda$  limits the mixing above the surface layer it could  
105 vary with stratification, a constraint we did not include explicitly. Note nevertheless that our calculations will cover  
106 a large range of  $\lambda$ , more stable cases being related to smaller values of this parameter. A difficulty with the mixing  
107 length profile in (8) is that the background flows that give uniform fluxes have a logarithmic contribution that extends  
108 up to  $z = \infty$  (see Eq. 1 in Belcher and Wood (1996)). As log-layers are confined to the near-surface and to simplify  
109 the theory, we slightly modify the formula for the mixing length in (8) and take,

$$\Lambda_0 = \lambda \tanh\left(\kappa \frac{Z+z_0}{\lambda}\right). \quad (9)$$

110 This approximation keeps  $\Lambda \approx \kappa Z$  near the surface and  $\Lambda \approx \lambda$  in the far field. With this expression, the horizontal  
111 wind and buoyancy profiles that give uniform fluxes are

$$U_V(Z) = \frac{u_*}{\kappa} \log\left(\frac{\sinh \kappa(Z+z_0)/\lambda}{\sinh \kappa z_0/\lambda}\right), \quad B_V(Z) = \frac{b_*}{\kappa} \log\left(\frac{\sinh \kappa(Z+z_0)/\lambda}{\sinh \kappa z_0/\lambda}\right). \quad (10)$$

112 where the subscript  $V$  denotes the background "viscous" solutions,  $u_* = \sqrt{\tau_s/\rho_s}$  is the friction velocity, and  $b_* =$   
113  $g H_s/(\rho_s c_p u_* \theta_s)$  is the buoyancy scale, with  $\tau_s$  and  $H_s$  for surface stress and heat flux and  $c_p$  for the air heat capacity  
114 per unit mass at constant pressure.

115 Another difficulty when one tries to analyse the interaction between mountain waves and a dissipative surface  
116 layer is that the velocity in (10) keeps increasing with altitude which is not realistic. The vertical profiles also tend to  
117 confine vertically propagating gravity waves to low altitudes. This can spuriously limit the contribution of the gravity  
118 waves to the Reynolds stress for instance. To circumvent this issue, we will consider cases where the wind profile is  
119 modified to become constant above a height  $d$

$$U_0(Z) = \frac{u_* d}{\lambda} \tanh\left[\frac{\lambda}{u_* d} U_V(Z)\right], \quad B_0(Z) = B_V(z). \quad (11)$$

120 This introduces a boundary layer depth  $d$  above which the background flow is externally imposed rather than being  
121 an exact solution of the viscous equations. Note that the case with infinite winds in the far field (10) can be obtained  
122 with (11) by taking  $d = \infty$ .

123 As an illustrative example Fig. 1 shows the background wind profiles for  $d = 1$  km and  $d = \infty$  in a configuration  
 124 that is characteristic for the cases we will analyse. For mountainous areas, typical values for roughness length, the  
 125 limit value of the mixing length, friction velocity, boundary layer depth and the mountain length scale are

$$z_0 = 1 \text{ m}, \lambda = 20 \text{ m}, u_* = 0.2 \text{ m.s}^{-1}, d = 1000 \text{ m}, L = 1000 \text{ m}. \quad (12)$$

126 The choice for  $z_0$  corresponds to that often made over chaotic surfaces (Wieringa, 1992) whereas that for  $\lambda$  is consis-  
 127 tent with observations (Sun, 2011). In Fig. 1a) one sees that when  $d = \infty$ ,  $U_0$  has constant shear over almost the entire  
 128 domain whereas when  $d = 1$  km, the constant shear zone is limited to the boundary layer where  $z < d$ . Henceforth  
 129 we will call cases using  $d = \infty$  "constant shear" cases and cases using  $d \neq \infty$  "variable shear" cases. Note that to  
 130 analyse cases where all harmonics propagate aloft, we will also consider hydrostatic solutions when  $d \neq \infty$ .

131 The zoom near the surface in Fig. 1b) shows that, when approaching the surface, the background wind transitions  
 132 from a linear profile to a log-profile around  $z = \lambda$ . We will call the logarithmic domain of the profile the surface layer.  
 133 Figure 1a) and 1b) also show the linear asymptote of  $U_0$  when  $\lambda \ll z \ll d$ , illustrating that

$$U_0(z) \underset{\lambda \ll z \ll d}{\approx} \frac{u_*(z + z_a)}{\lambda}, \quad B_0(z) \underset{\lambda \ll z}{\approx} \frac{b_*(z + z_a)}{\lambda} \quad (13)$$

134 where the parameter,

$$z_a = z_0 - \frac{\lambda}{\kappa} \log \left( 2 \sinh \frac{\kappa z_0}{\lambda} \right), \quad (14)$$

135 measures the depth of the "critical level": at  $z = -z_a$  all disturbances have null intrinsic phase speed. At least in the  
 136 boundary layer and above the surface layer, these asymptotes match  $U_0$  and  $B_0$  quite well. An important measure of  
 137 the flow stability is the background flow Richardson number,

$$Ri(z) = \frac{B_{0z}}{U_{0z}^2}, \quad (15)$$

138 From the flow profiles in (11), it is clear that  $Ri(z)$  is zero near the surface, constant and equal to parameter  $J$  in the  
 139 shear zone, and infinite when  $z \gg d$ . Parameter  $J$  is defined as

$$J = Ri(\lambda \ll z \ll d) = \lambda \frac{b_* u_*}{u_*^3} = \frac{\lambda}{\kappa L_{mo}}, \quad (16)$$

140 where  $L_{mo}$  is the Obukhov length. While in principle the characteristic length  $\lambda$  should be related to  $L_{mo}$ , we have  
 141 chosen to keep them separated in order to disentangle the dynamical impact of  $J$  through the inviscid dynamics and  
 142 of the turbulence (and hence  $\lambda$  or  $z_0$ ) through the near-surface dissipation. In the remaining part of this paper,  $J$  will  
 143 be called the Richardson number for short and will be used to control the stability regime.

## 144 2.2 | Inner scales and turning points

145 According to many papers about turbulent flows over gentle hills, it is often necessary to separate in the analysis three  
 146 different layers separated by the inner layer scale and the turning level defined in (1) and (2) respectively (Belcher  
 147 and Wood (1996)). If we replace  $L$  by the horizontal wavenumber  $k^{-1}$  and take for the eddy diffusivity acting on

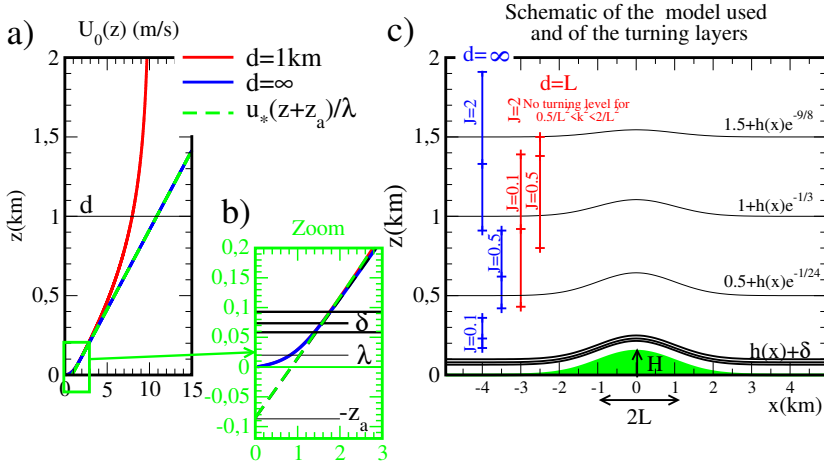


**FIGURE 1** a) and b) Background winds used and their various fits according to layer properties (see legend)  $\lambda = 20\text{m}$ ,  $z_0 = 1\text{m}$ ,  $L = 1\text{km}$ ,  $d = 1\text{km}$ ,  $u_* = 0.2\text{m/s}$ . c) Schematic of the model used. The 3 thin black solid lines follow the surfaces  $Z = 0.5, 1, 1.5$ . In b) and c) the thick black almost horizontal lines span the inner layer scales corresponding to the dominant harmonics excited by a Gaussian mountain ridge of horizontal scale  $L$ . In c) the vertical lines indicate the location and depth of the turning layer spanned by the turning levels according to (2): cases with  $d = \infty$  ( $d=L$ ) are in blue (red). The central crosses are for the dominant wavenumber  $k = 1/L$ .

148 disturbances  $v' = 2\Lambda u_*$ , (1) becomes

$$kU_0(\delta) \approx \frac{2\Lambda(\delta)u_*}{\delta^2}. \quad (17)$$

149 We have verified that it is very well approximated by

$$\delta(k) = \left(\frac{\lambda^2}{k}\right)^{1/3}, \quad (18)$$

150 an expression that facilitates the asymptotic development as a function of the small parameter  $\lambda/L$  presented in the  
 151 Appendix. The turning points are often located above the inner layer scale, at a height  $h_t$  defined by (2) again replacing  
 152  $L$  by  $k^{-1}$ . Their presence quantifies wave trapping, whereas the parameter  $J$  quantifies the depth over which trapping  
 153 occurs. To illustrate these points, here and in the rest of the paper we will consider Gaussian ridges with characteristic  
 154 horizontal scale  $L$ ,

$$h(x) = He^{-\frac{x^2}{2L^2}}, \quad (19)$$

155 with  $H$  the maximum mountain height. For such profile a large fraction of the excited harmonics have wavenumbers  
 156 that span the interval  $2^{1/2}/L < k < 2^{-1/2}/L$ . The corresponding interval in  $\delta$  is shown in Fig. 1b), illustrating that the inner  
 157 layer scales satisfy  $\lambda < \delta(k) < d$ . In panel 1c), this band of inner layer scales is also shown following the mountain  
 158 profiles.

159 Panel 1c) shows the vertical space spanned by the turning points,  $h_t$ , and for the cases with  $d = \infty$  (blue) and  $d = L$

160 (red) after implicit resolution of Eq. 2 and replacing  $1/L$  by  $2^{1/2}/L < k < 2^{-1/2}/L$  again. As in Part II one sees that in the  
 161 constant shear case ( $d = \infty$  blue vertical lines) the parameter  $J$  controls the altitude of the turning levels: when  $J < 1$   
 162 ( $J > 1$ ) the turning layer is predominantly below (above)  $L = 1$  km and we can expect a neutral (stratified) behaviour.  
 163 Note also that using the linear-log profiles for  $U_V$  and  $B_V$  derived from the more classical Blackadar formula (8), the  
 164 above diagnostics of inner layer and turning points do not differ much quantitatively.

165 In the variable shear case with  $d = L$  (red vertical lines), the turning points altitude also increases with  $J$  but are  
 166 located significantly higher than when  $d = \infty$ . Furthermore, when  $J$  approaches 1 and becomes larger, there are not  
 167 many waves trapped (there is almost no turning level for  $J = 2$ ). In these cases with fixed  $d = L$ , the fraction of  
 168 propagating versus trapped waves is measured by comparing the Scorer parameter in the far field to  $1/L^2$ : where we  
 169 have used the buoyancy profile in (10) and the wind profile in (11).  $F_r$  is a conventional Froude number, controlling  
 170 the amount of drag that can be transported by gravity waves in the far-field (Teixeira et al., 2013b). It is very likely that  
 171 it impacts the surface drag, an effect that we will only measure indirectly here and by comparing the cases  $F_r = \sqrt{J}$  to  
 172 cases with  $F_r = 0$  (constant shear) and  $F_r = \infty$  (hydrostatic). In other words, when  $d = L$  we have to keep in mind that  
 173  $J$  controls both the depth of the trapping region and the significance of trapping. In the present paper we emphasize  
 174 the first aspect and leave to a subsequent paper a more systematic analysis where both the depth of the trapping  
 175 region and the amount of trapping change separately.

### 176 2.3 | non-dimensional formulation

177 To integrate our equations using boundary layer techniques we start by deriving a non-dimensional form of (4) using  
 178 the scalings

$$(X, Z) = L(\bar{X}, \bar{Z}), (U_0, u, w, W) = \frac{u_* L}{\lambda} (\bar{U}, \bar{u}, \bar{w}, \bar{W}), \rho = u_*^2 \frac{L^2}{\lambda^2} \bar{\rho}, (B_0, b) = u_*^2 \frac{L}{\lambda^2} (\bar{B}, \bar{b}). \quad (20)$$

179 All the length scales characterizing the boundary layer depth and turbulent mixing become,

$$d = L\bar{d}, \delta = L\bar{\delta}, h_t = L\bar{h}_t, \lambda = L\bar{\lambda}, z_0 = L\bar{z}_0, \Lambda_0 = \lambda\bar{\Lambda}. \quad (21)$$

180 According to (9) the last scaling makes  $\bar{\Lambda}(\bar{z}) \approx O(1)$  which permits to write set (4) as

$$\rho (\bar{u} \partial_{\bar{X}} \bar{u} + \bar{W} \partial_{\bar{Z}} \bar{u}) = - (\partial_{\bar{X}} \rho \bar{p} + \partial_{\bar{Z}} \rho g^{12} \bar{p}) + \bar{\lambda}^2 \partial_{\bar{Z}} (\bar{\Lambda}^2 \|\partial_{\bar{Z}} \bar{u}\| \partial_{\bar{Z}} \bar{u}), \quad (22a)$$

181

$$\rho (\bar{u} \partial_{\bar{X}} \bar{w} + \bar{W} \partial_{\bar{Z}} \bar{w}) = - \partial_{\bar{Z}} \bar{p} + \rho \bar{b} + \bar{\lambda}^2 \partial_{\bar{Z}} (\bar{\Lambda}^2 \|\partial_{\bar{Z}} \bar{u}\| \partial_{\bar{Z}} \bar{w}), \quad (22b)$$

182

$$\rho (\bar{u} \partial_{\bar{X}} \bar{b} + \bar{W} \partial_{\bar{Z}} \bar{b}) = \bar{\lambda}^2 \partial_{\bar{Z}} (\bar{\Lambda}^2 \|\partial_{\bar{Z}} \bar{u}\| \partial_{\bar{Z}} \bar{b}), \quad (22c)$$

183

$$\partial_{\bar{X}} \rho \bar{u} + \partial_{\bar{Z}} \rho \bar{W} = 0, \quad (22d)$$



184 and makes explicit that the small parameter controlling the inner layer dynamics is  $\bar{\lambda}^2$ . Still in non-dimensional form,  
 185 coordinate transform (3) writes

$$\bar{x} = \bar{X}, \quad \bar{z} = \bar{Z} + \bar{h}(\bar{X})f(\bar{Z}) = \bar{Z} + \bar{z}'. \quad (23)$$

186 The following choice is made for the low hill and the vertical scaling function

$$\bar{h}(\bar{x}) = S e^{-\frac{\bar{x}^2}{2}}, \quad \text{and } f(\bar{Z}) = \exp\left(-\bar{Z}^3/3\right), \quad (24)$$

187 where  $S = H/L$  is the mountain slope. In (24) the definition of  $f(\bar{Z})$  is such that at the surface,  $f(0) = 1$ ,  $\dot{f}(0) = 0$ ,  
 188 and  $\ddot{f}(0) = 0$ , properties that permit to simplify the formalism in the inner layer.

## 189 2.4 | Linear analysis

190 If we consider hills of small slope  $S$ , we can assume that the response to the forcing terms is linear and consider  
 191 solutions of the form,

$$\bar{u} = \bar{U} + \bar{u}', \quad \bar{w} = \bar{w}'; \quad \bar{W} = \bar{W}', \quad \bar{\rho} = \bar{P} + \bar{\rho}', \quad \bar{b} = \bar{B} + \bar{b}', \quad \bar{z} = \bar{Z} + \bar{z}' \quad \text{and } \rho = 1 + \rho', \quad (25)$$

192 with normalized backgrounds,

$$\bar{U}(\bar{Z}) = \bar{d} \tanh \left[ \frac{\bar{\lambda}}{\kappa \bar{d}} \log \left( \frac{\sinh \kappa (\bar{Z} + \bar{z}_0)/\bar{\lambda}}{\sinh \kappa \bar{z}_0/\bar{\lambda}} \right) \right], \quad (26a)$$

193

$$\bar{B}_{\bar{Z}} = J \coth \left( \kappa (\bar{Z} + \bar{z}_0)/\bar{\lambda} \right), \quad (26b)$$

194

$$\bar{\lambda}(\bar{Z}) = \tanh(\kappa (\bar{Z} + \bar{z}_0)/\bar{\lambda}). \quad (26c)$$

195 We then search solutions in the form of Fourier transforms:

$$\bar{u}'(\bar{X}, \bar{Z}) = \int_{-\infty}^{+\infty} \bar{\mathbf{u}}(\bar{k}, \bar{Z}) e^{i\bar{k}\bar{X}} d\bar{k}. \quad (27)$$

196 Denoting  $\bar{\rho}$  and  $\bar{z}$  the Fourier transform of  $\rho'$  and  $\bar{z}'$  defined in (25), equations (22) linearize to

$$i\bar{k}\bar{U}\bar{\mathbf{u}} + \bar{U}_{\bar{Z}}\bar{\mathbf{W}} + i\bar{k}\bar{\mathbf{p}} - \bar{\lambda}^2 \partial_{\bar{Z}} 2\bar{\lambda} \partial_{\bar{Z}} \bar{\mathbf{u}} = i\bar{k}\bar{B}\bar{\mathbf{z}} \quad (28a)$$

197

$$i\bar{k}\bar{U}\bar{\mathbf{W}} + \partial_{\bar{Z}} \bar{\mathbf{p}} - \bar{\mathbf{b}} - \bar{\lambda}^2 \partial_{\bar{Z}} \bar{\lambda} \partial_{\bar{Z}} \bar{\mathbf{w}} = \bar{\rho}\bar{B} + \bar{k}^2 \bar{U}^2 \bar{\mathbf{z}}, \quad (28b)$$

198

$$i\bar{k}\bar{U}\bar{\mathbf{b}} + \bar{B}_{\bar{Z}}\bar{\mathbf{W}} - \bar{\lambda}^2 \partial_{\bar{Z}} \left( \bar{\lambda} \partial_{\bar{Z}} \bar{\mathbf{b}} + J\bar{\lambda} \partial_{\bar{Z}} \bar{\mathbf{u}} \right) = 0, \quad (28c)$$

$$ik\bar{u} + \partial_{\bar{z}}\bar{W} = -ik\bar{U}\bar{\rho}, \quad (28d)$$

$$\text{where } \bar{W} - \bar{w} = -ik\bar{U}\bar{z}, \quad (28e)$$

The no-slip boundary condition  $\bar{U}(0) = \bar{B}(0) = 0$  translates into

$$\bar{u} = \bar{W} = \bar{b} = 0. \quad (29)$$

## 2.5 | Rationale of the theoretical model and relation with earlier studies

As expected with terrain following coordinates, Eqs. (28) contain forcing terms associated to the metric, all of which are placed at the right hand side. In Appendix A.1 we compute the solutions of the homogeneous equations (28) and in Appendix A.2, we compute a particular solution that equilibrates these forcings. Both solutions are used to formulate a complete solution that matches the boundary conditions. For both the homogeneous solution and the particular solution we separate the domain of integration between an "inner layer" and an "outer layer", separated by a matching region where we derive asymptotic solutions that are valid in the lower part of the outer layer and upper part of the inner layer. The homogeneous and particular solutions have exact analytical solutions in both the outer and matching regions, the solutions in the inner layer being evaluated numerically starting from solutions in the matching region. Importantly, the numerical integration starts from near  $5\delta$  down to the surface, a numerical choice that is consistent with conventional viscous boundary layer theory where the inner layer depth, above which dissipation has less than 1% impact at leading order, is around 5 times the inner layer scale (see also Part I, II, and III).

To a large extent, equations (28) and their inner layer approximation derived in the Appendix (see Eqs. 62) are similar to Eqs. (16)-(19) in Belcher and Wood (1996), and to the basic equations in other papers using linear theory in curved coordinates (Beljaars et al., 1987; Weng et al., 1997). In terms of dynamics nevertheless, there is one important difference with Belcher and Wood (1996): we do not consider explicitly the presence of an almost inviscid middle layer where the Scorer parameter (2) is dominated by the background wind curvature. The reason is that our numerical integration starts from around  $5\delta$ , which corresponds to altitudes where the background wind curvature is small (in the "matching region", the background gradients are almost constant). To appreciate better the significance of the middle layer in our case, we have followed Eqs (2.2) in Hunt et al. (1988b), translate them in non-dimensional form and calculate the middle layer scale as the highest altitude  $\bar{h}_m$  below which,

$$\left\| \frac{\bar{U}_{\bar{z}\bar{z}}}{\bar{U}} \right\| \gg 1 \quad \text{and} \quad \left\| \frac{\bar{U}_{\bar{z}\bar{z}}}{\bar{U}} \right\| \gg \frac{\bar{B}_{\bar{z}}}{\bar{U}^2}, \quad (30)$$

and always found that  $0 < \bar{h}_m < 2\bar{\delta}$  with  $\bar{h}_m \approx 0$  when  $J$  is large and  $\bar{h}_m \approx 2\bar{\delta}$  when  $J$  is small (not shown). The middle layer scale is either near the inner layer scale, or does not even exist (for cases when  $\bar{h}_m < \bar{\delta}$ , see Hunt et al. (1988b)). This is in contrast with the altitude of the turning levels, which are often well above  $\bar{\delta}$  when  $J \neq 0$  (see Fig. 1c). In other words, our model potentially presents a large region between the inner scale and the turning points that can support the vertical propagation of internal gravity waves, these waves will fully interact with the turning levels and the inner layer yielding trapped lee waves that gradually attenuate downstream. This plus the intrinsic interest of providing uniform approximations are the major originalities of our work. Apart from these, our model is consistent

230 with the truncated mixing length model for turbulence adopted in the theory exposed in Belcher and Wood (1996)  
 231 because it neglects the impact of turbulence above the inner layer consistent with the rapid-distortion mechanism.

### 232 3 | WAVE FIELD AND TRANSITION FROM DOWNSTREAM SHELTERING TO 233 UPSTREAM BLOCKING

#### 234 3.1 | Wave field

235 To construct the solutions of Eqs. (27)-(28), we consider a very large periodic domain in the horizontal, e.g.  $50 < \bar{X} < 50$   
 236 sampled by 1024 points yielding a spectral resolution  $d\bar{k} \approx 0.06$ . The resolution in the vertical is refined near the  
 237 surface when needed: typically, we set  $d\bar{z} \approx S/10$  near the surface (actually more for plotting purposes rather  
 238 than for precision). Indeed, the solutions derived in Appendix are analytical in the outer and matching regions (see  
 239 Eqs. (41)-(49)-(52) for the homogeneous solution and (60)-(61) for the particular solution). Hence, when the numerical  
 240 integrations are carried out in the inner layer (A.1.3 for the homogeneous solution and A.2.3 for the particular solution)  
 241 we use an adaptive vertical step to minimize the error. After being evaluated on the curved grid, the solutions are  
 242 linearly interpolated on the rectangular grid, the vertical velocity  $\bar{w}'$  being expressed out of  $\bar{W}'$  according to (28e). In  
 243 all panels representing the velocity fields, we take for parameter values (12) and slope  $S = 0.2$ , their non dimensional  
 244 counterpart being given in the caption of Fig. 2. Note that we will also systematically vary the non-dimensional  
 turbulent lengths  $\bar{\lambda}$  and  $\bar{z}_0$  to test the sensitivity of our results to these two parameters.

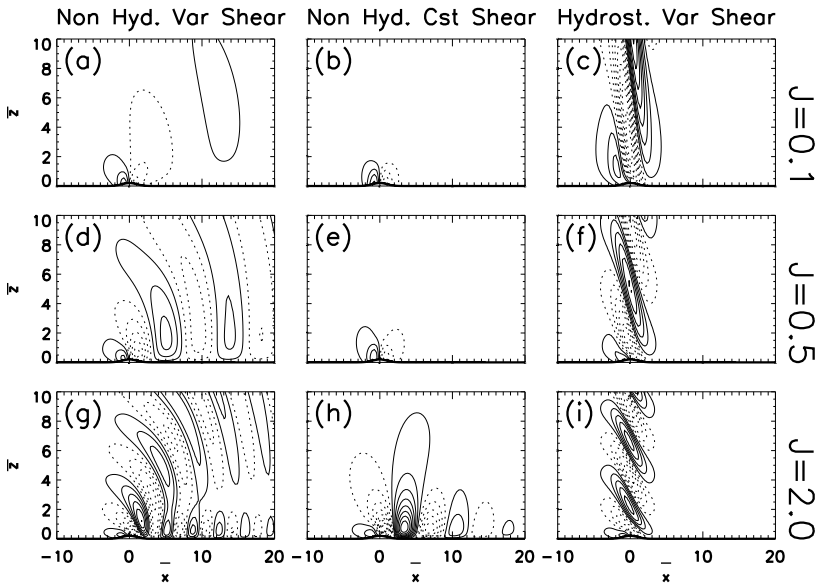


**FIGURE 2** Non dimensional vertical velocity field  $\bar{w}'$  for a mountain of slope  $S = 0.2$ , and boundary layer flow with mixing length  $\bar{\lambda} = 0.02$  (corresponding inner layer  $\bar{\delta} \approx 0.07$ ) and roughness length  $\bar{z}_0 = 0.001$  (depth of the critical layer  $\bar{z}_c \approx 0.16$ ). The boundary layer depth  $\bar{d} = 1$  except in (b) (e) and (h) where  $\bar{d} = \infty$ . Contour interval  $CI = 0.01$  with negative values dashed. Note that all these patterns have been validated with the non-linear model used in Lott et al. (2020b) (not shown).

245 We plot in Fig. 2 the vertical velocity field  $\bar{w}'$  when the outer flow has variable shear (left column), constant  
 246 shear (middle column), and variable shear with the hydrostatic approximation (right column). In each case, we present  
 247 results for increasing values of the Richardson number (from top to bottom). In the left column panels, harmonics with  
 248 wavenumber  $\bar{k} > \sqrt{J}$  encounter a turning height above which they are evanescent (see Eqs. (41)-(42) when  $\bar{d} = 1$ ).  
 249 In the middle column panels, all harmonics encounter a turning height. In the right column panels there is no turning  
 250 point: all harmonics propagate upward when  $\bar{z} \rightarrow \infty$ .

251 A first interesting aspect to notice is that the typical amplitude of the vertical velocity right on the windward side  
 252 of the hill is near  $\bar{U}(\bar{\delta}/2)S \approx 0.04$ , which is the amplitude of the vertical velocity produced when an inviscid flow of  
 253 speed  $\bar{U}(\bar{\delta}/2)$  passes over a ridge of slope  $S$  (note that the contour interval in each panel stays the same at 0.01). This  
 254 situation is very similar to the constant viscosity case discussed in Part I, where dissipative effects force streamlines,  
 255 up to  $\bar{z} = \bar{\delta}/2$ , to be displaced vertically over a distance  $S$ , such that at  $\bar{z} = \bar{\delta}/2$ , the vertical velocity should scale as  
 256  $\bar{U}(\bar{\delta}/2)S$ .

257 If we now look for similarities with previous constant viscosity studies, we conclude that the solutions with vari-  
 258 able wind in the first column are similar to those shown in Part III. In the near neutral case (Fig. 2a) almost no waves  
 259 develop aloft because most harmonics encounter a turning height and perhaps because the resonant modes have  
 260 longer horizontal wavelength than those predominantly excited by (19) (as in Part III and anticipating results in a sub-  
 261 sequent paper). In contrast, when  $J = 0.5$  in Fig. 2d, trapped waves dominate the response, because many harmonics  
 262 still encounter turning altitudes, whereas near resonant modes have shorter horizontal wavelength. The response be-  
 263 comes dominated by upward propagating waves when  $J = 2$  in Fig. 2g. This occurs because less harmonics encounter  
 264 turning height but there is also a system of trapped lee waves developing downstream.

265 The solutions with constant shear in the second column are characterized by very weak waves up to  $J = 0.5$   
 266 (Figs. 2b and 2e) which is a consequence of the facts that (i) all harmonics encounter turning heights in the vertical, (ii)  
 267 the turning heights are located near the surface (around  $\bar{h}_t \approx \sqrt{J}$ ) and (iii) upward waves cannot fully develop. When  $J$   
 268 increases further in Fig. 2h, trapped lee waves start to develop. They have two origins, the first is that in this case the  
 269 gravity waves have more room to propagate vertically before returning to the surface downstream (see Part II), and  
 270 the second is that the waves returning to the surface are less absorbed than in the constant viscosity case permitting  
 271 downward propagation. A more complete analysis of the trapped waves will be given in a subsequent paper, but the  
 272 onset of trapped waves when the wind shear becomes constant is reminiscent of the inviscid solutions with constant  
 273 wind shear and non-zero wind at the surface in Keller (1994).

274 The hydrostatic solutions in the right column present purely vertically propagating waves, as expected from  
 275 Eq. (43), the vertical wavelength decreasing with  $J$ .

## 276 3.2 | Downstream sheltering versus upstream blocking

277 To characterize the near surface flow, we plot in Fig. 3 the wind perturbation caused by the hill, normalized by the  
 278 incident wind and the total wind vector (background plus perturbation) in the quasi neutral and stratified cases shown  
 279 in Figs. 2a and 2g. The neutral case in Fig. 3a shows a relative augmentation in wind amplitude above the hill top  
 280 compared to the upstream flank, and an intensification above the hill crest that is characteristic of neutral flow over  
 281 hills. Still in the near-neutral case, the wind amplitude along the downstream flank is also reduced compared to the  
 282 upstream flank, a behaviour characterizing non-separated sheltering and produced by enhanced surface friction and  
 283 dissipation as the air travels across the ridge. Note nevertheless that the sheltering effect is much less pronounced  
 284 than in the constant viscosity case, a behaviour that naturally follows from the decrease of the diffusion coefficient

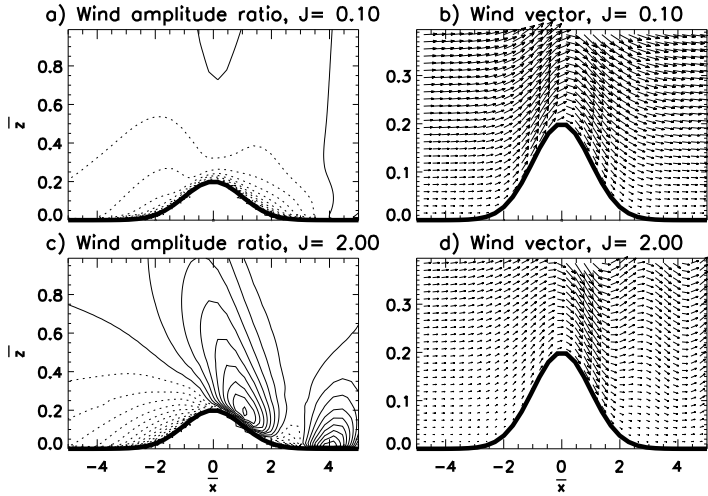


**FIGURE 3** Near mountain velocity fields with the same parameters as in Figs. 2(b) and 2(h). The panels (a) (c) on the left are for the total wind amplitude normalized by the background wind,  $\sqrt{u^2 + w^2}/\bar{U}(z)$ . The contour interval is 0.1 with values below 0 in dash. The panels on the right are for the total wind vector  $\bar{u}, \bar{w}$ .

285 when approaching the surface (compare Fig. 3b here and Fig. 6b in Part II).

286 In the stratified case in Figs. 3c and 3d the upslope/downslope asymmetry is much more pronounced: there is  
 287 strong wind intensification on the downstream side, with strong downslope winds penetrating well into the inner  
 288 layer. On the upstream side there is also pronounced deceleration, a process that we called non-separated blocking  
 289 in Part II.

290 We analyze more systematically the transition from neutral to stratified flow according to the downslope/upslope  
 291 asymmetry (i.e. following Part III) in Fig. 4. We plot the ratio between the downslope wind intensity and upslope wind  
 292 intensity,

$$\frac{\text{Max}_{\bar{z} < \frac{2S}{3}, 0 < \bar{x} < 2} \sqrt{u^2 + w^2}}{\text{Max}_{\bar{z} < \frac{2S}{3}, -2 < \bar{x} < 0} \sqrt{u^2 + w^2}}, \quad (31)$$

293 as a function of the Richardson number  $J$ . We also systematically vary the value of the mixing length  $\bar{\lambda}$  between 0.005  
 294 and 0.05, a range of variation that permits to satisfy  $\bar{\delta} \ll 1$  and to keep the dimensional values of  $\lambda$  of the order of  
 295 20 m and below when the the dimensional hill length varies between 200 m <  $L$  < 5 km. In order to be consistent with  
 296 our asymptotic analysis, we have to keep the roughness length  $\bar{\lambda}/2 < \bar{z}_0 < \bar{\lambda}/40$ , and to keep  $\bar{z}_a = O(\bar{\delta})$ ,  $\bar{z}_a$  being  
 297 controlled by the ratio  $\bar{z}_0/\bar{\lambda}$  (see Eq. 14). Physically, it means that our calculations are only valid if the depth of the  
 298 critical level  $\bar{z}_a$  compares with the inner layer scale. In practice we found that we should always satisfy the criterion  
 299  $5\bar{\delta} - \bar{z}_a > 0$  to have inner solutions that converge.

300 For almost all values of the dissipation parameters, Fig. 4 shows that the transition from neutral to stratified  
 301 behaviour occurs for  $J \approx 0.5$ , almost as in Part III (see Fig. 7b there). The sheltering is nevertheless less pronounced,  
 302 the ratio (31) falling below 0.5 in the constant viscosity case when  $J \ll 1$  and for  $S = 0.15$ , whereas it is always  
 303 between 0.5 and 1 for a larger slope ( $S = 0.2$ ). Again this is related to the fact that here, dissipative effects are smaller

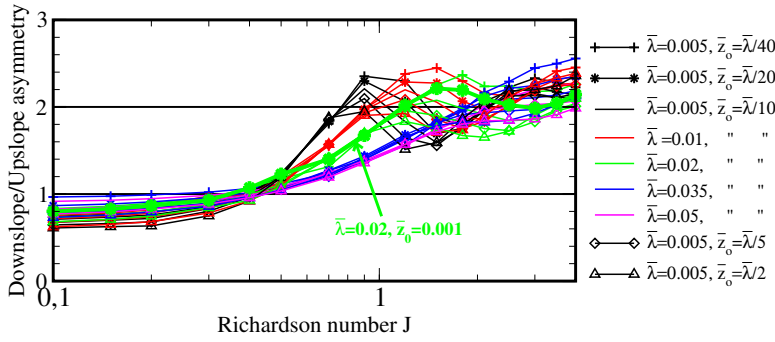


**FIGURE 4** Downslope sheltering versus upstream blocking index defined as the ratio between the max downslope wind amplitude and the max upslope wind amplitude (see Eq. (31)). Non-hydrostatic cases with variable shears,  $S = 0.2$ , and for values of  $\bar{\lambda}$  and  $\bar{z}_0$  shown in the legend.

304 near the surface when compared to the constant viscosity case.

## 305 4 | WAVES STRESS AND MOUNTAIN DRAG

### 306 4.1 | Pressure drag and Momentum fluxes

307 To appreciate the action of the wave on the large-scale flow, we next use a momentum budget in curved coordinates  
308 by averaging in  $\bar{X}$  the Boussinesq equation (22a) written in flux form,

$$\frac{\partial \bar{\rho} \bar{u}}{\partial t} = \frac{\partial}{\partial Z} \left( \underbrace{-\bar{\rho} \bar{u} \bar{W} + \bar{\rho} \partial_{\bar{X}} \bar{z} + \bar{\tau}_{\bar{X}Z}}_{\bar{\tau}_{\text{wav}}} \right), \quad (32)$$

309 where we have "re-"introduced a "large-scale" tendency on the left hand side to emphasize that we will use the  
310 stationary linear model to analyse the effect of the disturbances on the large-scale flow. This expression is appealing  
311 because the first two terms in the momentum flux on the RHS permit to capture smoothly the transition from mountain  
312 drag at  $Z = 0$  to the conventional "Eulerian mean" wave momentum flux when  $\bar{Z} \gg 1$  (e.g. where  $\bar{Z} = \bar{z}$ ). To a  
313 certain extent this expression has also a Lagrangian character. In the surface layer, the averaging is simply along the  
314 streamlines that follow the ridge making the average in good part Lagrangian by construction. Above the inner layer  
315 it follows that when dissipation is weak, the Reynolds stress alone equals the pressure torque along streamlines (see  
316 Eq. 23 in Part I when dissipation is small). In the following, we analyse the wave stress  $\bar{\tau}_{\text{wav}}$ , which is the contribution  
317 of our linear solutions to the sum of these two terms, after verification that the second order contribution to the  
318 dissipative stress  $\bar{\tau}_{\bar{X}Z}$ ,  $(\bar{\lambda} \bar{\lambda}' \bar{z}')^2$ , is significantly smaller than the wave stress in the inner layer.

319 Figure 5a shows the surface pressure drag as a function of  $J$  in the variable shear case ( $\bar{d} = 1$ ) and for the different  
320 values of the parameters  $\bar{\lambda}$  and  $\bar{z}_0$ . The pressure drag is divided by  $S^2$ , simply because we diagnose a quadratic term  
321 from a theory that is linear in  $S$ . On it, we see that the curves spread over a very large range of values and that the  
322 drag has a systematic tendency to increase with  $J$ . This is the classical behaviour where gravity wave drag gradually  
323 replaces the form drag due to non-separated sheltering and when the trapping region becomes thicker (Yu and Teixeira,

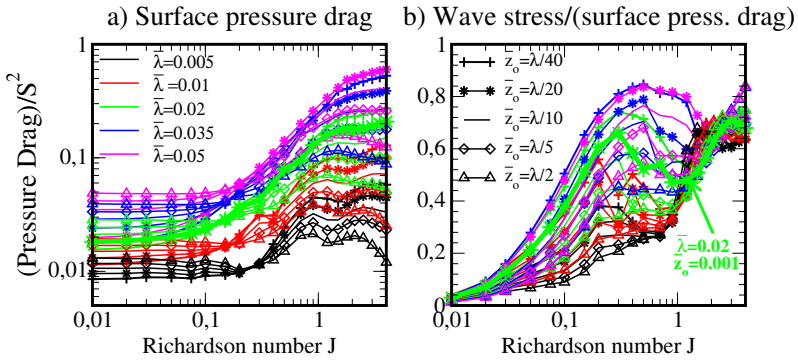


**FIGURE 5** Mountain drag and wave momentum flux divided by  $S^2$  in the non-hydrostatic variable shear case and for different values of  $\bar{\lambda}$  and  $\bar{z}_0$ . a) Mountain drag  $\bar{\tau}_{wav}(\bar{Z} = 0)$ ; b): Ratio between wave stress in the far field and at the mountain drag ( $\bar{\tau}_{wav}(\bar{Z} = \infty)/\bar{\tau}_{wav}(\bar{Z} = 0)$ ).

2015). There is also a tendency for the drag to increase with  $\bar{\lambda}$ . As the incident wind at the inner layer scale  $\bar{U}(\bar{\delta})$  increases with  $\lambda$  (not shown) this is consistent with our results in Part I where we show that it is the incident wind at the inner layer scale that controls the drag amplitude.

The dependence of the drag on  $\bar{z}_0$  is related to flow stability. In the neutral case, say for  $J < 0.5$ , the drag increases with roughness ("triangles" are above "plus signs") simply because there is more dissipation, making the sheltering more pronounced ("triangles" are below "plusses" in Fig. 4). The situation reverses in the stratified case ( $J > 0.5$ ) where the drag decreases when the roughness length increases. An interpretation could be that when  $\bar{z}_0$  increases,  $\bar{z}_a$  decreases, i.e. the critical level gets closer to the surface, which makes that the waves are more attenuated by the enhancement of the dissipative effects that occur near critical levels (Booker and Bretherton, 1967). As in these cases the drag is dominated by wave drag, enhanced wave dissipation could result in decreased wave drag.

In Fig. 5b, we plot the ratio between the wave stress in the far field and the surface pressure drag. Without a surprise, one sees that for small  $J$ , most of the pressure drag is deposited at low levels (typically about 80% when  $J \lesssim 0.1$ ), which is a natural consequence of the fact that most harmonics are evanescent in the vertical and in the far field. At the other extreme for the stable cases, a good fraction of the drag radiates in the far field (about 70% when  $J > 1$ ), with only 30% of the surface drag being eroded by dissipation. Finally, the transition region, say for  $0.1 < J < 1$ , is remarkably rich in terms of variations in this ratio. When we look at the vertical velocity fields in Fig. 2 and compare the case with  $J = 0.5$  in Fig. 2e to the other less stable and more stable cases in Figs. 2b and 2h respectively, we see that the transition region is clearly dominated by trapped lee waves that do not contribute substantially to the momentum flux in the far-field. In this intermediate regime, we also observe a big variability in the momentum flux arriving in the far field. As an illustration, we see in Fig. 5b that for  $J = 0.3$ , about 20% of the drag becomes a momentum flux when ( $\bar{\lambda} = 0.005$ ,  $\bar{z}_0 = \bar{\lambda}/2$ ) (black line with triangles), whereas it is 80% when ( $\bar{\lambda} = 0.035$ ,  $\bar{z}_0 = \bar{\lambda}/10$ ) (blue line with diamonds).

Following the earlier suggestion that the incident velocity relevant for the drag must be measured at the inner layer scale, Fig. 6a shows the pressure drag divided by  $\bar{U}(\bar{\delta}/2) S^2$ , which is an estimate of the wave drag occurring for an incident flow of speed  $\bar{U}(\bar{\delta}/2) S^2$  when  $J = 1$ . We believe that this predictor could also work for the drag due to non-separated sheltering because it compares relatively well to  $\bar{\delta}\bar{u}(S)S$ , a measure of the drag associated with the pressure decrease across the hill that equilibrates surface friction (see Part II). With this normalization, one sees that

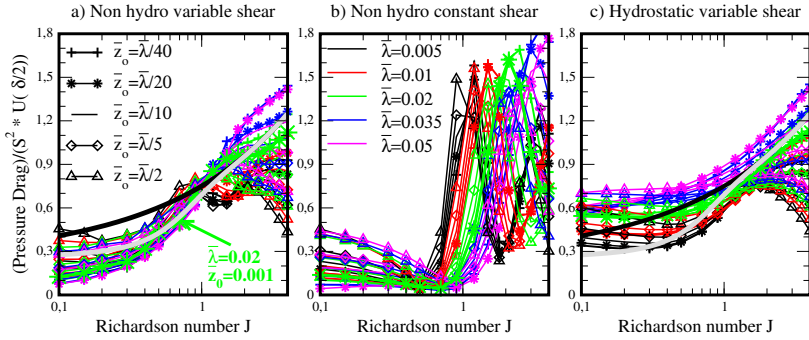


**FIGURE 6** Mountain drag divided by  $S^2 \bar{U}(\delta/2)$  and for different values of  $\bar{\lambda}$  and  $\bar{z}_0$ . The thick black and grey lines in a) and c) are for the rough estimates of the variations in drag with Richardson number discussed in Section 5 (see Eqs. (33) and (34) respectively).

351 the drag values remain on the order of magnitudes around 1 with smaller values in the neutral cases and larger values  
 352 in the stratified cases. The figure also illustrates well the transition around  $J = 1$ , with larger drag in the stratified case.  
 353 There is nevertheless a rich variability in drag as a function of  $\bar{z}_0$  and  $\bar{\lambda}$  when stability is large: we did not manage to  
 354 capture this variability with a simple predictor.

355 To emphasize the significance of the conditions of wave propagation aloft, we plot in Figs 6b and Figs 6c the drag  
 356 when all the waves are trapped (the non-hydrostatic case with constant shear) and free to propagate aloft (hydrostatic  
 357 with variable shear) respectively. When all the disturbances are trapped in Fig. 6b, the transition at  $J \approx 1$  is even more  
 358 pronounced than in Fig. 6a. In almost all cases, and when  $J$  varies between 0.5 and 1, the drag decreases before  
 359 increasing rapidly as  $J$  approaches 1. These rapid transitions occur for all values of  $\bar{\lambda}$  and  $\bar{z}_0$ , as was also seen in  
 360 the constant viscosity case. This variation is related to the interaction between the reflected waves and the surface  
 361 (yielding relatively low and high drag states (see also Teixeira et al. (2013a)). When all the waves can propagate aloft,  
 362 we observe the opposite behaviour (Fig. 6c, hydrostatic variable shear). The variations in drag with  $J$  are much less  
 363 dramatic than in the other two cases. Interestingly, one sees that for small  $J$  the pressure drag is larger than in Figs. 6a  
 364 and 6b, illustrating that allowing all the disturbances to propagate freely as gravity waves in the vertical direction  
 365 favors the drag. Of course this is academic, since only few disturbances can propagate vertically when  $J$  is small in  
 366 the non-hydrostatic case but it illustrates the general significance of the waves for the mountain drag.

367 Finally, Fig. 7 shows vertical profiles of the waves stress ( $\bar{\tau}_{wav}$  in Eq. 32) in the nine cases presented in Fig. 2. As  
 368 expected we see a decrease with altitude of the momentum flux, which typically occurs over a depth near  $\bar{Z} \approx 3\bar{\delta} \approx 0.2$ .  
 369 The fact that such a decrease occurs inside the inner layer depth  $5\bar{\delta}$  is systematic, but the exact depth is somehow  
 370 dependent on the critical level depth  $\bar{z}_a$  (and hence  $\bar{z}_0$ ) (not shown). We see that the momentum flux decrease has two  
 371 causes: (i) the effect of wave trapping that always dominates the constant shear case (black curves) and (ii) the erosion  
 372 by dissipation of the waves when they travel upward through the inner layer and that is the only mechanism at work in  
 373 the hydrostatic case (about 15% to 20% erosion, see blue curves). In the non-hydrostatic case with variable shear, one  
 374 sees that the two effects contribute almost equally. For instance in the stratified case ( $J = 2$ ), the red and blue dotted  
 375 curves show that the decrease of the stress in the inner layer is two to three times larger in the non-hydrostatic case  
 376 than in the hydrostatic one. The contribution of the trapped waves to the momentum flux decay equals and exceeds  
 377 the erosion of the freely propagating waves.



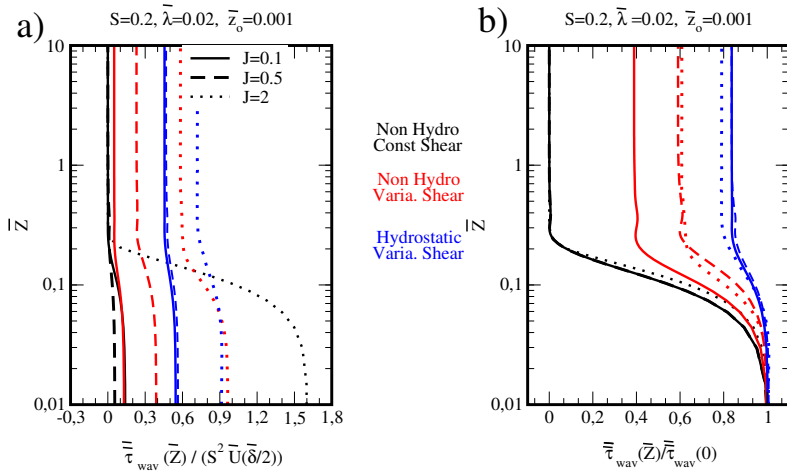


**FIGURE 7** Momentum flux vertical profiles according to Eq. 32 and for the 9 cases in Fig.2. Panels on the left and right are identical except the stress profiles in (b) are divided by the surface value to emphasize erosion with altitude.

## 378 5 | SUMMARY AND DISCUSSION

379 In dynamical meteorology and oceanography, boundary layer turbulence is often parameterized with an eddy diffusivity  
 380 in order to capture the interaction between the surface and the boundary layer. Although these types of closure  
 381 are today questioned, for instance because the smallest scales of turbulence can backscatter on the large scales  
 382 (Schumann and Launder, 1995; Weinbrecht and Mason, 2008), or in mountaneous areas, because the turbulence is  
 383 notoriously non-homogeneous in the horizontal direction (Stiperski and Rotach, 2016), many numerical models still  
 384 use them. It seems therefore essential to provide theory that could help explain the behaviour of these models, e.g.  
 385 the system of mountain waves developing in a boundary layer parameterized by a classical mixing length closure.

386 This type of study could also provide some guidance to develop parameterization of subgrid scale orography for  
 387 at least two reasons. The first is that parameterizations of subgrid scale mountains are rooted in linear theories that  
 388 depict (i) the interaction between the boundary layer and subgrid scale orography using eddy diffusivity closure, and  
 389 (ii) the generation of mountain waves in the stratified case neglecting the boundary layer (except that the large-scale  
 390 flow that enters in the evaluation of the wave drag is impacted by the boundary layer). The second is that the transition  
 391 between stratified and neutral flow can seemingly be characterized by near resonant trapped lee waves which are not  
 392 well parameterized in models. The present paper provides some answers to help developing a parameterization that  
 393 encompasses all the scales of the SSO. The first answer is that it suggests that the incident wind value at the inner layer  
 394 scale should be used to measure the drag (or average over the inner layer, see normalisation in Fig. 6). In a large-scale  
 395 model that uses a viscosity type closure, and for a given mountain length, this height can be diagnosed by comparing  
 396 the amplitude of the disturbance advection with dissipation (according to Eq. 1). With our mixing length model closure  
 397 this is well approximated by  $\delta = L^{1/3} \lambda^{2/3}$  as in Eq. (18) with  $k = 1/L$ . The second answer is that the nature of the drag  
 398 (i.e. mountain drag due to non-separated sheltering versus gravity wave drag) has to be decided above the inner layer.  
 399 This is very important because it can be done without requesting information about the properties of the turbulence  
 400 itself: we just have to find, for a given mountain length  $L$  the turning point altitude  $h_t$ , defined in Eq. 2, and compare  
 401 it to  $L$ . If  $h_t < L$  gravity waves have not enough space to develop in the vertical and the dynamics is neutral, if  $h_t > L$

402 the dynamics is stratified. More specifically, in the constant shear cases with the turning altitude at around  $h_t \approx \sqrt{J}L$ ,  
 403 small (large) values of  $J$  mean that the turning altitude is close to the surface (far from the surface) and we found  
 404 neutral (stratified) behaviour. In the variable shear case, the turning altitude is slightly above the surface for small  $J$   
 405 and substantially higher (up to the top of the atmosphere) for large  $J$  yielding about the same qualitative conclusions.  
 406 In contrast to Belcher and Wood (1996), we find that this turning altitude should not be used to evaluate the incident  
 407 wind that enters in the drag formula.

408 Making closed form predictions beyond the fact that the drag scales with  $\rho_s \left( \frac{u_* L}{\lambda} U(\delta/2) S^2 \right)$  turned out to be  
 409 quite difficult, so we did not propose any in the core of the paper. Nevertheless, we can suggest some attempts to  
 410 capture at least the  $J$  dependence. The first is

$$\left( \rho_s \frac{u_* L}{\lambda} U(\delta/2) S^2 \right) 0.25 * (1 + 2\sqrt{J}) , \quad (33)$$

411 where the first term in parenthesis is the dimensional form of the normalization used in Fig. 6, and the second term  
 412 is the sum of a form drag and a wave drag, as shown by the thick black curves in Fig. 6a and 6c. This fit is adapted  
 413 in the hydrostatic case when all disturbances becomes waves in the far field. It overestimates the drag in the neutral  
 414 case, where gravity waves should not play a role. So, to separate both regimes and allow a rapid transition from one  
 415 to the other we also plot in thick grey the predictor

$$\left( \rho_s \frac{u_* L}{\lambda} U(\delta/2) S^2 \right) * 0.25 * \left( 1 + \left( 1 + \tanh \left( \frac{(J - 0.5)}{0.5} \right) \right) \sqrt{J} \right) . \quad (34)$$

416 The tanh term in (34), limits the wave contribution in the neutral case and allows for a quite rapid transition from the  
 417 neutral to the stratified cases. The rapid increase in drag when  $J \approx 0.5$  is presumably related to trapped waves.

418 An important limitation of our work is nevertheless that we have focused on the depth of the trapping region and  
 419 less on the relative amount of waves that stay trapped (i.e. that are evanescent for  $z \rightarrow \infty$ ). This relative amount is  
 420 controlled by the inverse Froude number

$$F = \frac{U(\infty)}{N(\infty)L}, \quad (35)$$

421 which is well known to control the non-hydrostatic effect on the mountain wave drag. (Teixeira et al., 2013b). In the  
 422 constant shear case ( $F = \infty$ ), all the waves stay trapped; in the variable shear case ( $F = \frac{L}{d\sqrt{J}}$ ), the fraction of trapped  
 423 waves decreases when  $J$  increases because we always take  $d/L = 1$ ; and in the hydrostatic case ( $F \approx 0$ ), all the waves  
 424 propagate up. Accordingly, it is likely that the increase in drag with  $J$  in Figure 6a is due to the fact that more waves  
 425 can propagate up. To illustrate that this effect is at work in our results, we notice that when  $J$  is small ( $J \leq 0.5$ ) the  
 426 drag is larger in the variable shear case than when all the waves are trapped (Figure 6b) and smaller than when all  
 427 can propagate up (Figure 6a). In a companion paper, we do experiments where  $J$  only controls the free shear layer  
 428 stability not the amount of trapping, for instance leaving  $Fr$  constant by taking  $d = \frac{L}{\sqrt{J}}$ .

429 We are not going to speculate further on the application of our results except to formulate them in a way that  
 430 involve further the background flow at the dynamical levels we have identified. We can for example approximate  
 431 the wind factor  $\frac{u_* L}{\lambda}$  by  $U(h_t)$ , and interpret the Richardson number dependence in terms of  $\bar{h}_t$  the ratio between the  
 432 turning heights and the mountain length in which case, the drag predictor (33) can be roughly approximated by

$$\rho_s U(h_t) U(\delta/2) S^2 * \bar{h}_c^{-2} * (1 + \bar{h}_t / \bar{h}_c) \quad \text{where } \bar{h}_t = \frac{h_t}{L}, \quad (36)$$

433  $\bar{h}_c = 0.5$  being a critical value. In all these formula one should replace  $\bar{h}_t$  by the "normalized" boundary layer depth  
 434  $\bar{d}$  when it is larger. This formula could be compared to (72) and (73) in Belcher and Wood (1996), the slope  $S$  being  
 435 replaced by  $Hk$  and  $\bar{h}_t$  by the inverse of a Froude number ( $Fr_t = \frac{U(h_t)}{LN(\bar{h}_t)}$ ). According to the above discussion concerning  
 436 the potential role of the Froude numbers on the dynamics and drag we leave this issue to further analysis. In this paper,  
 437 the most significant difference we identify is that one of the two background wind values in (36) is to be taken near  
 438 the inner layer scale (i.e. in  $\delta/2$ ) not at the turning altitude  $h_t$ . Nevertheless, the most important similarity is that in  
 439 both formulations, the nature of the dynamics (neutral or stratified) has to be decided at the turning height.

## 440 A | MIXED THEORETICAL FINITE DIFFERENCE MODEL

441 To solve the set of equations (28) over a semi infinite domain we combine theoretical inviscid solutions and numerical  
 442 solutions in the inner layer, the inner layer scale varying for each harmonics according to:

$$\bar{\delta}(\bar{k}) = \left( \frac{\bar{\lambda}^2}{\bar{k}} \right)^{1/3}. \quad (37)$$

443 The matching between the inviscid or "outer layer" solution will be made in a matching region in which analytical  
 444 asymptotic solutions are also derived. These "matching" solutions will permit to initialize the dissipative equations at  
 445  $\bar{z} \approx 5\bar{\delta}$ , which is relatively near the ground, and integrate them down to the surface to give the "inner solutions". The  
 446 uniform solutions are combinations of these three "outer", "matching" and "inner" solutions, they will be evaluated  
 447 for both the homogeneous solution and the particular solution. The derivation of the matching solutions is central to  
 448 our study, because in them one can identify those asymptoting the inviscid solution, and which are the Booker and  
 449 Bretherton (1967) solutions, and those with exponential growth with altitude and which are purely due to dissipations.  
 450 The fact that they have exponential growth explains why the system we analyse is almost impossible to integrate  
 451 numerically from  $\bar{z} \approx \infty$  to the surface.

### 452 A.1 | Homogeneous solution

#### 453 A.1.1 | Outer solution

454 When  $\bar{\lambda} \ll 1$  and without the right hand side terms, the set of equations (28) reduce to the homogeneous inviscid  
 455 equations. We will use this approximation where  $\bar{z} \gg \bar{\delta}$ , and as  $\bar{\delta} > \bar{\lambda}$ , they can be solved using the background  
 456 profiles approximated by

$$\bar{U} \approx \bar{d} \tanh \frac{\bar{z} + \bar{z}_a}{\bar{d}}, \quad \bar{B} \approx J(\bar{z} + \bar{z}_a). \quad (38)$$

457 For such profiles the inviscid homogeneous part of (28) satisfies the Taylor-Goldstein equation,

$$\frac{d^2 \bar{W}}{d\bar{z}^2} + \left( \frac{J}{\bar{U}^2} + \frac{2}{\bar{d}^2} \left( 1 - \frac{\bar{U}^2}{\bar{d}^2} \right) - \bar{k}^2 \right) \bar{W} = 0, \quad (39)$$

458 which solutions can be expressed in terms of Haenkel functions when  $\bar{d} = \infty$  or hypergeometric functions when  $\bar{d} \neq \infty$   
 459 (i.e. the solution named  $\bar{w}_I$  given Eq. (12) in Part II and Eq. (13) in Part III respectively). The only difference with Part II

460 and Part III is that the critical level is at  $Z = -\bar{z}_a$  rather than at  $Z = 0$ , a behaviour that is transparent when we write  
 461 the asymptotic forms

$$\bar{W}_I(\bar{z}) = \bar{w}_I(\bar{k}, \bar{z} + \bar{z}_a) \underset{\bar{z} \rightarrow \infty}{\approx} e^{-\bar{m}(\bar{z} + \bar{z}_a)}, \quad (40)$$

$$\underset{\bar{z} \rightarrow 0}{\approx} \bar{a}_1 (\bar{z} + \bar{z}_a)^{1/2 - i\mu} + \bar{a}_2 (\bar{z} + \bar{z}_a)^{1/2 + i\mu} = \bar{W}_{IM}, \quad (41)$$

462 where the  $\bar{a}_1$  and  $\bar{a}_2$  are given by (13) in Part II when  $\bar{d} = \infty$  and by (A12) in Part III when  $\bar{d} \neq \infty$ . Still in (41),

$$\mu = \sqrt{\left|J - \frac{1}{4}\right|}, \text{ and } \bar{m} = \sqrt{\left|\bar{k}^2 - J/\bar{d}^2\right|}, \quad (42)$$

463 when  $J > 1/4$  and  $\bar{k}^2 \bar{d}^2 > J$  respectively. When  $J < 1/4$ ,  $\mu$  is changed in  $i\mu$  and when  $\bar{k}^2 \bar{d}^2 < J$ ,  $\bar{m}$  is changed  
 464 in  $-i \text{sign}(\bar{k})\bar{m}$ . Solution (41) corresponds to a "unit amplitude" exponentially decaying mode when  $\bar{z} \rightarrow \infty$  (or re-  
 465 sumeard propagating wave when  $\bar{m}$  is imaginary). Near the surface (41) behaves like the linear combinations of the  
 466 near critical level solutions of Booker and Bretherton (1967), the critical level being located below the surface (at  
 467  $Z = -\bar{z}_a$ ). The function  $\bar{W}_{IM}$  in (41) is a matching function that will play a central role in the build up of uniform  
 468 approximations.

469 Note finally that when the shear varies in the far field, the hydrostatic approximation is simply obtained by chang-  
 470 ing  $\bar{m}$  in (42) by

$$\bar{m} = -i \text{sign}(\bar{k})\sqrt{J/\bar{d}}. \quad (43)$$

### 471 A.1.2 | Matching region

472 An important aspect of our work is that there exists a matching region when  $\bar{z}$  is small but above the surface layer  
 473 where dissipative effects starts being significant. In this region, the background wind shear and stratification are almost  
 474 constant (in dimensional form see (13)) and we can find approximate form of the viscous solutions that will match the  
 475 outer solution and that will allow to initialise analytically the inner layer numerical integration. In this matching region,  
 476 the homogeneous parts of Eqs. (28) are approximated by

$$i\bar{k}(\bar{z} + \bar{z}_a)\bar{u} + \bar{W} + i\bar{k}\bar{p} - 2\bar{\lambda}^2 \partial_{\bar{z}} \partial_{\bar{z}} \bar{u} = 0. \quad (44a)$$

$$i\bar{k}(\bar{z} + \bar{z}_a)\bar{b} + J\bar{W} - \lambda^2 \partial_{\bar{z}} (\partial_{\bar{z}} \bar{b} + J \partial_{\bar{z}} \bar{u}) = 0, \quad (44b)$$

$$\partial_{\bar{z}} \bar{p} - \bar{b} = 0, \text{ and } i\bar{k}\bar{u} + \partial_{\bar{z}} \bar{W} = 0, \quad (44c)$$

479 which can be approximated by one 6<sup>th</sup> order equation for  $\bar{W}$ :

$$2\bar{\delta}^6 \bar{W}^{(6)} - 3i(\bar{z} + \bar{z}_a)\bar{\delta}^3 \bar{W}^{(4)} - (2 - J)i\bar{\delta}^3 \bar{W}^{(3)} - (\bar{z} + \bar{z}_a)^2 \bar{W}^{(2)} - J\bar{W} = 0. \quad (45)$$

480 To find asymptotic solutions we follow Koppel (1964) and try the WKB Ansatz,

$$\overline{W}(\overline{Z}) = A(\overline{Z} + \overline{z}_a) e^{\frac{\beta(\overline{Z} + \overline{z}_a)}{\epsilon}}, \quad (46)$$

481 where  $A$  and  $B$  are functions and  $\epsilon$  a small parameter. If we use that

$$\overline{W}^{(n)} \approx \left( \frac{A\dot{B}^n}{\epsilon^n} + n \frac{\dot{A}\dot{B}^{n-1}}{\epsilon^{n-1}} + \frac{n(n-1)}{2} \frac{A\ddot{B}\dot{B}^{n-2}}{\epsilon^{n-1}} + O(\epsilon^{2-n}) \right) e^{\beta/\epsilon}, \quad (47)$$

482 a choice that left non-degenerated (45) at the leading order is  $\epsilon = \overline{\delta}^{3/2}$ . In this case and at order  $\epsilon^{-2}$  one has:

$$2\dot{B}^6 - 3i(\overline{Z} + \overline{z}_a)\dot{B}^4 - (\overline{Z} + \overline{z}_a)^2\dot{B}^2 = 0. \quad (48)$$

483 This admits 3 solutions corresponding to disturbances that do not grow exponentially in the far field:

$$\dot{B} = 0, \quad \dot{B} = -\sqrt{i}\sqrt{\overline{Z} + \overline{z}_a}, \quad \text{and} \quad \dot{B} = -\sqrt{i/2}\sqrt{\overline{Z} + \overline{z}_a}.$$

484 When  $\dot{B} = 0$  all terms with powers in  $\overline{\delta}$  in (45) are small which give the two inviscid solutions of Booker and Bretherton  
485 (1967):

$$(\overline{Z} + \overline{z}_a)^{\frac{1}{2}-i\mu}, \quad (\overline{Z} + \overline{z}_a)^{\frac{1}{2}+i\mu}. \quad (49)$$

486 For  $\dot{B} \neq 0$  one needs to go to order  $\epsilon^{-1}$  and obtain:

$$\dot{A} \left( 12\dot{B}^5 - 12i(\overline{Z} + \overline{z}_a)\dot{B}^3 - 2(\overline{Z} + \overline{z}_a)^2\dot{B} \right)$$

487

$$+ A \left( 30\ddot{B}\dot{B}^4 - 18i(\overline{Z} + \overline{z}_a)\ddot{B}\dot{B}^2 - (2-J)i\dot{B}^3 - (\overline{Z} + \overline{z}_a)^2\ddot{B} \right) = 0. \quad (50)$$

488 After substitution of  $\dot{B}$  this gives

$$\frac{\dot{A}}{A} = -\frac{9+2J}{4(\overline{Z} + \overline{z}_a)} \quad \text{and} \quad \frac{\dot{A}}{A} = -\frac{5-2J}{4(\overline{Z} + \overline{z}_a)} \quad (51)$$

489 for  $\dot{B} = -\sqrt{i}\sqrt{\overline{Z} + \overline{z}_a}$ , and  $\dot{B} = -\sqrt{i/2}\sqrt{\overline{Z} + \overline{z}_a}$  respectively. This gives two other WKB solutions,

$$(\overline{Z} + \overline{z}_a)^{-\frac{9+2J}{4}} e^{-\frac{2}{3}\sqrt{i}\left(\frac{\overline{Z} + \overline{z}_a}{\overline{\delta}}\right)^{3/2}}; \quad (\overline{Z} + \overline{z}_a)^{-\frac{5-2J}{4}} e^{-\frac{2}{3}\sqrt{i/2}\left(\frac{\overline{Z} + \overline{z}_a}{\overline{\delta}}\right)^{3/2}}. \quad (52)$$

490 The inner solutions having these asymptotic behaviour do not need to be matched to the outer solution because they  
491 decay exponentially fast in the vertical, they are mandatory to satisfy the 3 no-slip surface conditions.

### 492 A.1.3 | Inner solutions

493 To evaluate the solution when  $\bar{Z} \rightarrow 0$ , we next introduce the inner layer scale and the inner variables,

$$\bar{\delta} = \left( \frac{\bar{\lambda}^2}{k} \right)^{1/3}, \quad \bar{Z} + \bar{z}_a = \bar{\delta} (\tilde{Z} + \tilde{z}_a), \quad \bar{W} = \bar{\delta} k \tilde{W}, \quad \bar{p} = \bar{\delta} \tilde{p}, \quad \bar{u} = \tilde{u}, \quad \bar{\mathbf{b}} = \tilde{\mathbf{b}}. \quad (53)$$

494 With these new variables and at leading order, the homogeneous part of (28) transforms into:

$$i\tilde{U}\tilde{u} + \tilde{U}_{\tilde{Z}}\tilde{W} = -i\tilde{p} + \partial_{\tilde{Z}} 2\tilde{\lambda} \partial_{\tilde{Z}} \tilde{u}, \quad (54a)$$

$$i\tilde{U}\tilde{\mathbf{b}} + J\tilde{U}_{\tilde{Z}}\tilde{W} = \partial_{\tilde{Z}} \tilde{\lambda} \left( \partial_{\tilde{Z}} \tilde{\mathbf{b}} + J\partial_{\tilde{Z}} \tilde{u} \right). \quad (54b)$$

$$\partial_{\tilde{Z}} \tilde{p} = \tilde{\mathbf{b}}, \quad \text{and} \quad i\tilde{u} + \partial_{\tilde{Z}} \tilde{W} = 0, \quad (54c)$$

497 Here, we have also written

$$U \approx \bar{\delta} \tilde{U}, \quad \text{where} \quad \tilde{U} = \frac{\tilde{\lambda}}{\kappa} \log \left( \frac{\sinh \kappa (\tilde{Z} + \tilde{z}_0) / \tilde{\lambda}}{\sinh \kappa \tilde{z}_0 / \tilde{\lambda}} \right), \quad \tilde{\lambda} = \tanh \left( \kappa \frac{\tilde{Z} + \tilde{z}_0}{\tilde{\lambda}} \right), \quad (55)$$

498 which take into account that in the inner layer  $\bar{U}$  scales as  $\bar{\delta}$  and  $\bar{U} \approx \bar{U}_V$ . As in Lott et al. (2020a) 3 solutions of  
499 (54) are evaluated numerically using a standard Runge-Kutta algorithm with adaptative vertical mesh, the integrations  
500 typically starting around  $\tilde{z} \approx 5$  initialized by the matching functions and integrated toward the surface.

501 More specifically, and to ensure the matching with the outer solution, we first evaluate the inner solution  $\tilde{W}_2$   
502 which almost coincides with the matching function  $\bar{W}_{IM}$  when  $\tilde{Z} \rightarrow \infty$ , i.e we initialize the integration with

$$\tilde{W}_2 \underset{\tilde{Z} \rightarrow \infty}{\approx} \tilde{a}_1 (\tilde{z} + \tilde{z}_a)^{1/2-i\mu} + \tilde{a}_2 (\tilde{z} + \tilde{z}_a)^{1/2+i\mu}, \quad \text{where} \quad \tilde{a}_1 = \frac{\bar{a}_1}{k} \bar{\delta}^{-1/2-i\mu}, \quad \tilde{a}_2 = \frac{\bar{a}_2}{k} \bar{\delta}^{-1/2+i\mu}. \quad (56)$$

503 Second and to permit to satisfy the 3 boundary conditions we also evaluate numerically the two solutions that are  
504 exponentially small in the far field, i.e. the two solutions  $\tilde{W}_3$  and  $\tilde{W}_4$  with asymptotic behaviours (52):

$$\tilde{W}_3 \underset{\tilde{Z} \rightarrow \infty}{\approx} (\tilde{Z} + \tilde{z}_a)^{-\frac{9+2J}{4}} e^{-\frac{2}{3}\sqrt{i}(\tilde{z}+\tilde{z}_a)^{3/2}}, \quad \text{and} \quad \tilde{W}_4 \underset{\tilde{Z} \rightarrow \infty}{\approx} (\tilde{Z} + \tilde{z}_a)^{-\frac{5-2J}{4}} e^{-\frac{2}{3}\sqrt{i}(\tilde{z}+\tilde{z}_a)^{3/2}}. \quad (57)$$

### 505 A.1.4 | Uniform approximations

506 Now that we have inner, matching and outer solutions, we can build uniform approximations out of the three, but all  
507 have to be written with the same coordinate. If we take the outer coordinate for instance, the uniform approximation  
508 for the vertical velocity of the outgoing solution can be written

$$\bar{W}_{2U}(\bar{Z}) = \bar{W}_I(\bar{Z}) + k\bar{\delta}\tilde{W}_2(\bar{Z}/\bar{\delta}) - \bar{W}_{IM}(\bar{Z}). \quad (58)$$

509 whereas the uniform approximations of the viscous solution corresponding to  $\bar{W}_3$  and  $\bar{W}_4$  simply consist in writing  
 510 them using outer coordinates, both functions becoming exponentially small in the outer layer (in this case, outer and  
 511 matching just coincide):

$$\bar{W}_{3U}(\bar{Z}) = \bar{k}\bar{\delta}\bar{W}_3(\bar{Z}/\bar{\delta}), \quad \bar{W}_{4U}(\bar{Z}) = \bar{k}\bar{\delta}\bar{W}_4(\bar{Z}/\bar{\delta}). \quad (59)$$

## 512 A.2 | Particular solution

### 513 A.2.1 | Outer solution ( $\bar{z} \gg \bar{\delta}$ )

514 When neglecting the viscous terms in (28), a particular solution is the linear approximation of the difference between  
 515 the backgrounds expressed in cartesian and curved coordinates (for the wind the difference  $\bar{U}(\bar{z}) - \bar{U}(\bar{Z})$ ), yielding

$$\bar{u}_{Ip} = \bar{z}\bar{U}_{\bar{z}}, \quad \bar{b}_{Ip} = \bar{z}\bar{B}_{\bar{z}}, \quad \bar{p}_{Ip} = \bar{z}\bar{B}(\bar{Z}), \quad \text{and} \quad \bar{W}_{Ip} = -i\bar{k}\bar{U}\bar{z}. \quad (60)$$

### 516 A.2.2 | Matching region

517 In the matching region, this solution is

$$\bar{u}_{Mp} = \bar{z}, \quad \bar{b}_{Mp} = J\bar{z}, \quad \bar{p}_{Mp} = J(\bar{Z} + \bar{z}_a)\bar{z}, \quad \text{and} \quad \bar{W}_{Mp} = -i\bar{k}(\bar{Z} + \bar{z}_a)\bar{z}. \quad (61)$$

### 518 A.2.3 | Inner region

519 In the inner region, we use the scalings (53) and (55) yielding at leading order,

$$i\bar{U}\bar{u} + \bar{U}_{\bar{z}}\bar{W} + i\bar{p} - \partial_{\bar{z}}2\bar{\lambda}\partial_{\bar{z}}\bar{u} = i\bar{B}\bar{h}, \quad (62a)$$

520

$$\partial_{\bar{z}}\bar{p} - \bar{b} = 0, \quad (62b)$$

521

$$i\bar{U}\bar{b} + \bar{B}_{\bar{z}}\bar{W} - \partial_{\bar{z}}\bar{\lambda}\left(\partial_{\bar{z}}\bar{b} + J\partial_{\bar{z}}\bar{u}\right) = 0, \quad (62c)$$

522

$$i\bar{u} + \partial_{\bar{z}}\bar{W} = 0. \quad (62d)$$

523 The particular solution is obtained through numerical integration of Eqs. (62) initialized by the particular solution  
 524 matching function (61). If we call  $\bar{W}_{Vp}(\bar{k}, \bar{Z})$  the solution, an uniform expression of the particular solution can be  
 525 written

$$\bar{W}_{Up}(\bar{k}, \bar{Z}) = \bar{W}_{Ip}(\bar{k}, \bar{Z}) + \bar{k}\bar{\delta}\bar{W}_{Vp}(\bar{k}, \bar{Z}/\bar{\delta}) - \bar{W}_{Mp}(\bar{k}, \bar{Z}), \quad (63)$$

526 with similar expressions for  $\bar{u}_{Up}$  and  $\bar{b}_{Up}$ .

### 527 A.3 | Boundary conditions

528 We then re-write the complete flow fields combining linearly the three homogeneous uniform solutions and the par-  
529 ticular uniform solution,

$$\overline{W}(\overline{X}, \overline{Z}) = \int_{-\infty}^{+\infty} \left( f_2(\overline{k}) \overline{W}_{2U}(\overline{k}, \overline{Z}) + f_3(\overline{k}) \overline{W}_{3U}(\overline{k}, \overline{Z}) + f_4(\overline{k}) \overline{W}_{3U}(\overline{k}, \overline{Z}) + \overline{W}_{pU}(\overline{k}, \overline{Z}) \right) e^{i\overline{k}\overline{X}} d\overline{k}, \quad (64)$$

530 with similar expressions for  $\overline{u}$ ,  $\overline{b}$  and  $\overline{p}$ . With this notation, the surface conditions (29) give,

$$f_2(\overline{k}) \overline{W}_{2U}(\overline{k}, 0) + f_3(\overline{k}) \overline{W}_{3U}(\overline{k}, 0) + f_4(\overline{k}) \overline{W}_{4U}(\overline{k}, 0) = -\overline{W}_{Up}(0), \quad (65)$$

531 with similar expression for  $\overline{u}$  and  $\overline{b}$ . The 3 relations obtained for each  $\overline{k}$  permit to evaluate the coefficients  $f_i(\overline{k})$  and  
532 reconstruct the wave field after inverse Fourier transform and interpolation on the rectangular grid.

### 533 references

- 534 Allen, T. and Brown, A. (2002) Large-eddy simulation of turbulent separated flow over rough hills. *Boundary-Layer Meteorology*,  
535 **102**, 177–198.
- 536 Ambaum, M. and Marshall, D. (2005) The effects of stratification on flow separation. *Journal of the Atmospheric Sciences*, **62**,  
537 2618–2625.
- 538 Belcher, S. E. and Wood, N. (1996) Form and wave drag due to stably stratified turbulent flow over low ridges. *Quart. J. Roy.*  
539 *Meteor. Soc.*, **122**, 863–902.
- 540 Beljaars, A., Walmsley, J. and Taylor, P. (1987) A mixed spectral finite-difference model for neutrally stratified boundary-layer  
541 flow over roughness changes and topography. *Boundary-Layer Meteorology*, **38**, 273–303.
- 542 Beljaars, A. C. M., Brown, A. R. and Wood, N. (2004) A new parametrization of turbulent orographic form drag. *Quarterly*  
543 *Journal of the Royal Meteorological Society*, **130**, 1327–1347.
- 544 Boegman, L. and Stastna, M. (2019) Sediment resuspension and transport by internal solitary waves. *Annual Review of Fluid*  
545 *Mechanics*, **51**, 129–154.
- 546 Booker, J. R. and Bretherton, F. P. (1967) The critical layer for internal gravity waves in a shear flow. *J. Fluid Mech.*, **27**, 102–109.
- 547 Chimonas, G. and Nappo, C. J. (1989) Wave drag in the planetary boundary layer over complex terrain. *Boundary-layer mete-*  
548 *orology*, **47**, 217–232.
- 549 Clark, T. L. (1977) A small-scale dynamic model using a terrain-following coordinate transformation. *Journal of Computational*  
550 *Physics*, **24**, 186–215.
- 551 Durran, D. R. (1990) Mountain waves and downslope winds. *AMS Meteorological Monographs*, **23**, 59–83.
- 552 Finnigan, J., Ayotte, K., Harman, I., Katul, G., Oldroyd, H., Patton, E., Poggi, D., Ross, A. and Taylor, P. (2020) Boundary-layer  
553 flow over complex topography. *Boundary-Layer Meteorology*, **177**, 247–313.
- 554 Hunt, J. C. R., Leibovich, S. and Richards, K. J. (1988a) Turbulent shear flows over low hills. *Quart. J. Roy. Meteor. Soc.*, **114**,  
555 1435–1470.
- 556 Hunt, J. C. R., Richards, K. J. and Brighton, P. W. M. (1988b) Stably stratified shear flow over low hills. *Quart. J. Roy. Meteor.*  
557 *Soc.*, **114**, 859–886.



- 558 Keller, T. L. (1994) Implications of the hydrostatic assumption on atmospheric gravity waves. *Journal of the atmospheric sciences*,  
559 51, 1915–1929.
- 560 Koppel, D. (1964) On the stability of flow of a thermally stratified fluid under the action of gravity. *Journal of Mathematical*  
561 *Physics*, 5, 963–982.
- 562 Lott, F., Deremble, B. and Soufflet, C. (2020a) Mountain waves produced by a stratified boundary layer flow. part i: Hydrostatic  
563 case. *Journal of the Atmospheric Sciences*, 77, 1683–1697.
- 564 – (2020b) Mountain waves produced by a stratified shear flow with a boundary layer. part ii: Form drag, wave drag, and  
565 transition from downstream sheltering to upstream blocking. *Journal of the Atmospheric Sciences*.
- 566 Lott, F. and Miller, M. (1997) A new subgrid scale orographic drag parameterization; its testing in the ecmwf model. *Quart. J.*  
567 *Roy. Meteor. Soc.*, 123, 101–127.
- 568 Palmer, T. N., Shutts, G. J. and Swinbank, R. (1986) Alleviation of systematic westerly bias in general circulation and numerical  
569 weather prediction models through an orographic gravity wave drag parametrization. *Quart. J. Roy. Meteor. Soc.*, 112,  
570 2056–2066.
- 571 Pokharel, B., Geerts, B., Chu, X. and Bergmaier, P. (2017) Profiling radar observations and numerical simulations of a downslope  
572 wind storm and rotor on the lee of the medicine bow mountains in wyoming. *Atmosphere*, 8, 39.
- 573 Reinert, D., Wirth, V., Eichhorn, J. and Panhans, W.-G. (2007) A new large-eddy simulation model for simulating air flow and  
574 warm clouds above highly complex terrain. part i: The dry model. *Boundary-layer meteorology*, 125, 109–132.
- 575 Richard, E., Mascart, P. and Nickerson, E. C. (1989) The role of surface friction in downslope windstorms. *J. Appl. Meteor.*, 28,  
576 241–251.
- 577 Ross, A., Arnold, S., Vosper, S., Mobbs, S., Dixon, N. and Robins, A. (2004) A comparison of wind tunnel experiments and  
578 simulations of neutral and stratified flow over a hill. *Boundary-Layer Meteorology: an international journal of physical and*  
579 *biological processes in the atmospheric boundary layer*, 113, 427 – 459.
- 580 Sachsperger, J., Serafini, S. and Grubisic, V. (2015) Lee waves on the boundary-layer inversion. *Frontiers in Geophysics*, Submitted.  
581
- 582 Sauer, J. A., Muñoz-Esparza, D., Canfield, J. M., Costigan, K. R., Linn, R. R. and Kim, Y.-J. (2016) A large-eddy simulation study of  
583 atmospheric boundary layer influence on stratified flows over terrain. *Journal of the Atmospheric Sciences*, 73, 2615–2632.
- 584 Schumann, U. and Launder, B. E. (1995) Stochastic backscatter of turbulence energy and scalar variance by random subgrid-  
585 scale fluxes. *Proceedings of the Royal Society of London. Series A: Mathematical and Physical Sciences*, 451, 293–318.
- 586 Smith, R. B., Jiang, Q. and Doyle, J. D. (2006) A theory of gravity wave absorption by a boundary layer. *J. Atmos. Sci.*, 63,  
587 774–781.
- 588 Soontiens, N., Stastna, M. and Waite, M. L. (2015) Topographically generated internal waves and boundary layer instabilities.  
589 *Physics of Fluids*, 27, 086602.
- 590 Soufflet, C., Lott, F. and Deremble, B. (2022) Mountain waves produced by a stratified shear flow with a boundary layer. part  
591 iii: Trapped lee waves and horizontal momentum transport. *Journal of the Atmospheric Sciences*, 79, 1601 – 1614.
- 592 Stiperski, I. and Rotach, M. W. (2016) On the measurement of turbulence over complex mountainous terrain. *Boundary-Layer*  
593 *Meteorology*, 159, 97–121.
- 594 Sun, J. (2011) Vertical variations of mixing lengths under neutral and stable conditions during cases-99. *Journal of Applied*  
595 *Meteorology and Climatology*, 50, 2030–2041.

- 596 Teixeira, M. A. C., Argain, J. L. and Miranda, P. M. A. (2013a) Orographic drag associated with lee waves trapped at an inversion.  
597 *J. Atmos. Sci.*, **70**, 2930–2947.
- 598 Teixeira, M. A. C., Argain, J. L. and Miranda, P. M. A. (2013b) Drag produced by trapped lee waves and propagating mountain  
599 waves in a two-layer atmosphere. *Quarterly Journal of the Royal Meteorological Society*, **139**, 964–981.
- 600 Tsiringakis, A., Steeneveld, G.-J. and Holtslag, A. (2017) Small-scale orographic gravity wave drag in stable boundary layers  
601 and its impact on synoptic systems and near-surface meteorology. *Quarterly Journal of the Royal Meteorological Society*,  
602 **143**, 1504–1516.
- 603 Voigt, M. and Wirth, V. (2013) Mechanisms of banner cloud formation. *Journal of the Atmospheric Sciences*, **70**, 3631–3640.
- 604 Vosper, S. B., Brown, A. R. and Webster, S. (2016) Orographic drag on islands in the nwp mountain grey zone. *Quarterly Journal*  
605 *of the Royal Meteorological Society*, **142**, 3128–3137.
- 606 Weinbrecht, S. and Mason, P. J. (2008) Stochastic backscatter for cloud-resolving models. part i: Implementation and testing  
607 in a dry convective boundary layer. *Journal of the Atmospheric Sciences*, **65**, 123–139.
- 608 Weng, W., Chan, L., Taylor, P. and Xu, D. (1997) Modelling stably stratified boundary-layer flow over low hills. *Quarterly Journal*  
609 *of the Royal Meteorological Society*, **123**, 1841–1866.
- 610 Wieringa, J. (1992) Updating the davenport roughness classification. *Journal of Wind Engineering and Industrial Aerodynamics*,  
611 **41**, 357–368. URL: <https://www.sciencedirect.com/science/article/pii/016761059290434C>.
- 612 Wood, N., Brown, A. and Hewer, F. (2001) Parameterizing the effects of orography on the boundary layer: an alternative to  
613 effective roughness lengths. *Quart. J. Roy. Meteor. Soc.*, **127**, 759–777.
- 614 Wood, N. and Mason, P. (1993) The pressure force induced by neutral, turbulent flow over hills. *Quart. J. Roy. Meteor. Soc.*,  
615 **119**, 1233–1267. 206,1 96
- 616 Yu, C. L. and Teixeira, M. C. (2015) Impact of non-hydrostatic effects and trapped lee waves on mountain-wave drag in direc-  
617 tionally sheared flow. *Quarterly Journal of the Royal Meteorological Society*, **141**, 1572–1585.